Transport phenomena in laser surface alloying

S. SARKAR*, P. MOHAN RAJ*, S. CHAKRABORTY*, G. PHANIKUMAR‡,
K. CHATTOPADHYAY‡, P. DUTTA*,§
*Department of Mechanical Engineering and ‡Metallurgy,
Indian Institute of Science, Bangalore 560 012, India
E-mail: pradip@mecheng.iisc.ernet.in

A three dimensional, transient model is developed for studying heat transfer, fluid flow and mass transfer for the case of a single-pass laser surface alloying process. The numerical study is performed in a co-ordinate system fixed to the laser which moves with a constant scanning speed. The coupled momentum, energy and species conservation equations are solved using a finite volume technique. Phase change processes are modelled using a fixed-grid enthalpy-porosity technique, which is capable of predicting the continuously evolving solid-liquid interface. The three-dimensional model is able to predict the species concentration distribution inside the molten pool during alloying, as well as in the entire cross section of the solidified alloy. Corresponding experimental results show a good qualitative agreement with the numerical predictions with regard to pool shape and final composition distribution. © 2003 Kluwer Academic Publishers

Nomenclature

a_p, a_p^0	Discretisation equation coefficients
c	Specific heat
D	Species mass diffusion coefficient
E	Activation energy
f_l	Liquid fraction of the solute
F^{-1}	Inverse of latent heat function
g	Acceleration due to gravity
h	Convective heat transfer coefficient
h_s	Sensible enthalpy
H	Total enthalpy
k	Thermal conductivity
k_p	Partition coefficient
L	Latent heat of fusion
m_f	Powder feedrate
$\dot{m}$	Mass flux
n	Normal direction
p	Pressure
q	Net power
q''	Heat flux
Q	Actual power input
r_q	Radius of heat input
R	Reference width of the pool
$\bar{R}$	Universal gas constant
S	Source term
T	Temperature
t	Time
$\vec{u}$	Velocity vector
u	x-component of velocity
u_{scan}	Laser scanning velocity
v	Y-component of velocity
v_n	Interface velocity
w	z-component of velocity

x'	x-coordinate in a fixed frame of reference
x, y, z	Co-ordinates fixed to the laser source

Greek symbols

β_T	Coefficient of volumetric expansion of heat
β_C	Coefficient of volumetric expansion of solute
η	Efficiency
Γ	Diffusion coefficient in general transport equation
ΔH	Latent enthalpy
ε	Emissivity
ϕ	General scalar variable
λ	Relaxation factor
σ	Surface tension
σ_T	Surface tension coefficient of temperature
σ_e	Stefan-Boltzmań constant
ρ	Density
μ	Viscosity

Subscripts

Al	Aluminium
$boil$	Boiling
Fe	Iron
max	Maximum value
m	Melting point
n	Iteration level/normal direction
old	Old iteration value
p	Nodal coefficient
ref	Reference

Superscripts

/	Stationary co-ordinate system

§Author to whom all correspondence should be addressed.

1. Introduction

Laser Surface alloying is a surface treatment used on metallic surfaces to apply a coating with improved surface properties on the top of a cheaper base material. Typically, it involves melting of a thin layer of base metal using a high power laser and simultaneously feeding an alloying element into the laser generated melt pool.

During laser surface alloying, as the heat source interacts with the metal substrate, several complex phenomena such as melting, mixing of powder feed, solidification, etc. occur. These processes influence the structure and properties of the alloyed region. It is expected that the melt pool flow, thermal and solidification characteristics will have a profound effect on the microstructure of the solidified region. Hence, it is desirable to develop a computational model which can simulate the entire physical process including heating, melting, mixing and solidification.

Heat and fluid flow in laser melted pools have been studied numerically by several researchers in the past [1–7]. Most of the above models employ two-dimensional or axi-symmetric models, to obtain insights on the behaviour of laser melted pools subjected to various process parameters. He *et al.* [7] presented one of the pioneering studies on laser surface alloying, in which mass transfer is taken into account in addition to heat transfer and fluid flow. In their study, a two-dimensional quasi-steady finite element model was applied to simulate single pass laser surface alloying of copper on aluminium base metal.

In the present study of laser surface alloying, we solve a set of transient, coupled, three-dimensional equations of mass, momentum, energy and species conservation using a fixed-grid, finite volume methodology with an enthalpy-porosity approach [8] to treat melting and solidification. The problem is formulated using a coordinate system moving with the laser. The transient formulation allows us to simulate the evolution of the pool geometry, which cannot be accurately captured by an iterative quasi-steady models often used in the previous studies in this field. The other main feature of the present model is its three-dimensionality, which appropriately represents a moving laser pool which is inherently three-dimensional. The three-dimensional model also allows us to obtain the pool cross sectional geometry (containing the width) and a final composition distribution in the entire solidified alloy, which are essential for comparison with the corresponding data from experimental post laser-processed sections. Such comparisons were not possible with previous two-dimensional models. The present study consists of alloying aluminium on an iron substrate. The numerical results are validated with corresponding experimental ones by comparing the pool cross sectional geometry and composition distribution in the solidified alloy.

2. Mathematical modelling

Fig. 1 shows a schematic diagram of the laser surface alloying process. The laser moves with a constant scanning speed, u_{scan}, along the x-direction. The intense heat from the laser beam strikes the opaque surface of
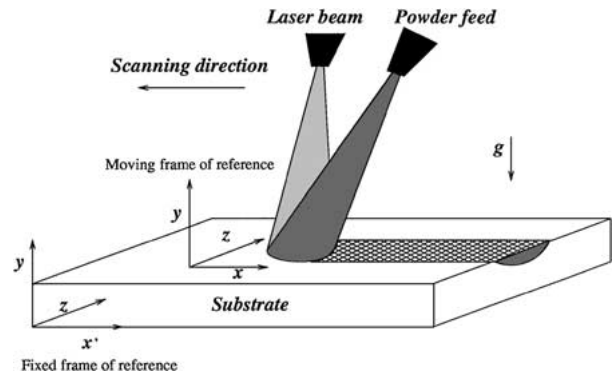

Figure 1 A schematic diagram of a typical laser surface alloying process.

the base metal. Only a part of the heat available from the laser beam heats the surface of the work-piece and leads to the formation of a molten pool. Hence, in the thermal modelling of laser surface alloying, the actual power, q, that goes into the work-piece as heat input is usually specified through a parameter, η, the laser beam efficiency, by the following relation:

$$q = \eta Q \qquad (1)$$

where Q represents the total laser power. As the pool reaches a completely molten state, an alloying element is added to the pool in the form of a powder. The powder melts and mixes with the molten base metal by convection and diffusion. As the laser source moves away from the location where the pool is already developed, resolidification of the zone occurs, leading to a final solidified micro-structure.

In the present formulation, the following assumptions are made: (i) the top surface of the pool remains flat, (ii) momentum transfer due to added powder particles is negligible, and (iii) the powder species exists as a dilute solution in the molten pool.

2.1. Governing equations

If (x', y, z) is a coordinate system in the stationary frame, then the generalised convection-diffusion equation in that frame can be written as:

$$\frac{\partial}{\partial t}(\rho\phi) + \frac{\partial}{\partial x'}(\rho u\phi) + \frac{\partial}{\partial y}(\rho v\phi) + \frac{\partial}{\partial z}(\rho w\phi)$$
$$= \frac{\partial}{\partial x'}\left(\Gamma\frac{\partial\phi}{\partial x'}\right) + \frac{\partial}{\partial y}\left(\Gamma\frac{\partial\phi}{\partial y}\right)$$
$$+ \frac{\partial}{\partial z}\left(\Gamma\frac{\partial\phi}{\partial z}\right) + S \qquad (2)$$

Since the molten pool moves with the laser beam, the problem is more conveniently studied in a reference frame fixed with the laser. Although a final quasi-steady state will be reached, we prefer to study it in a transient mode so as to predict the evolution of pool development. The final shape and size of the pool depends on this evolution, and hence it cannot be determined accurately by a direct quasi-steady formulation. If (x, y, z) is a Cartesian coordinate system fixed with the laser, the following transformation equations can be written.

$$x = x' - u_{scan}t \qquad (3)$$

156

where u_{scan} is the scanning speed of the laser. Differentiating Equation 3 with respect to t and noting that u_{scan} is a constant, we get:

$$u = u' - u_{scan} \qquad (4)$$

Using the above transformation equations, the governing equations in the moving frame can be written as [8]:

Continuity:

$$\frac{\partial}{\partial t}(\rho) + \nabla \cdot (\rho \vec{u}) = 0 \qquad (5)$$

X-momentum equation:

$$\frac{\partial}{\partial t}(\rho u) + \frac{\partial}{\partial x}(\rho u u) + \frac{\partial}{\partial y}(\rho u v) + \frac{\partial}{\partial z}(\rho u w)$$
$$= -\frac{\partial p}{\partial x} + \frac{\partial}{\partial x}\left(\mu \frac{\partial u}{\partial x}\right) + \frac{\partial}{\partial y}\left(\mu \frac{\partial u}{\partial y}\right)$$
$$+ \frac{\partial}{\partial z}\left(\mu \frac{\partial u}{\partial z}\right) + S_x - \frac{\partial}{\partial x}(\rho u_{scan} u) \qquad (6)$$

Y-momentum equation:

$$\frac{\partial}{\partial t}(\rho v) + \frac{\partial}{\partial x}(\rho u v) + \frac{\partial}{\partial y}(\rho v v) + \frac{\partial}{\partial z}(\rho v w)$$
$$= -\frac{\partial p}{\partial y} + \frac{\partial}{\partial x}\left(\mu \frac{\partial v}{\partial x}\right) + \frac{\partial}{\partial y}\left(\mu \frac{\partial v}{\partial y}\right)$$
$$+ \frac{\partial}{\partial z}\left(\mu \frac{\partial v}{\partial z}\right) - \frac{\partial}{\partial x}(\rho u_{scan} v) + \rho g \beta_T (T - T_{ref})$$
$$+ \rho g \beta_c (C - C_{ref}) + S_y \qquad (7)$$

Z-momentum equation:

$$\frac{\partial}{\partial t}(\rho w) + \frac{\partial}{\partial x}(\rho u w) + \frac{\partial}{\partial y}(\rho v w) + \frac{\partial}{\partial z}(\rho w w)$$
$$= -\frac{\partial p}{\partial z} + \frac{\partial}{\partial x}\left(\mu \frac{\partial w}{\partial x}\right) + \frac{\partial}{\partial y}\left(\mu \frac{\partial w}{\partial y}\right)$$
$$+ \frac{\partial}{\partial z}\left(\mu \frac{\partial w}{\partial z}\right) - \frac{\partial}{\partial x}(\rho u_{scan} w) + S_z \qquad (8)$$

where S_x, S_y and S_z are the porosity source terms, as in a standard enthalpy-porosity model described in [8].

Energy equation:

$$\frac{\partial}{\partial t}(\rho H) + \frac{\partial}{\partial x}(\rho u H) + \frac{\partial}{\partial y}(\rho v H) + \frac{\partial}{\partial z}(\rho w H)$$
$$= \frac{\partial}{\partial x}\left(k \frac{\partial T}{\partial x}\right) + \frac{\partial}{\partial y}\left(k \frac{\partial T}{\partial y}\right) + \frac{\partial}{\partial z}\left(k \frac{\partial T}{\partial z}\right)$$
$$- \frac{\partial}{\partial x}(\rho u_{scan} H) \qquad (9)$$

The enthalpy, H, of a material can be expressed as:

$$H = h_s + \Delta H \qquad (10)$$
$$h_s = c_T \qquad (11)$$

where h_s is the sensible heat, and ΔH is the latent heat content. In order to establish a mushy phase change,

the latent heat contribution is specified as a function of temperature, T, and the resulting expression is:

$$\Delta H = f(T) \qquad (12)$$

Since latent heat is associated with the liquid fraction, f_l, we can write:

$$\Delta H = f(T) \quad
\begin{aligned}
&= L &\text{for} \quad &T \geq T_l \\
&= f_l L &\text{for} \quad &T_s \leq T < T_l \\
&= 0 &\text{for} \quad &T < T_s
\end{aligned} \qquad (13)$$

where T_l is the liquidus temperature, T_s is the solidus temperature, and L is the latent heat of fusion. Substituting the expression for H from Equations 10 and 11 in the energy Equation 9, we arrive at the following final form of the energy equation:

$$\frac{\partial}{\partial t}(\rho c t) + \frac{\partial}{\partial x}(\rho c u T) + \frac{\partial}{\partial y}(\rho c v T) + \frac{\partial}{\partial z}(\rho c w T)$$
$$= \frac{\partial}{\partial x}\left(k \frac{\partial T}{\partial x}\right) + \frac{\partial}{\partial y}\left(k \frac{\partial T}{\partial y}\right) + \frac{\partial}{\partial z}\left(k \frac{\partial T}{\partial z}\right)$$
$$- \frac{\partial}{\partial x}(\rho u_{scan}(cT + \Delta H)) + S_e \qquad (14)$$

where S_e is the source term in the energy equation which can be written as:

$$S_e = -\frac{\partial}{\partial t}(\rho \Delta H) - \nabla \cdot (\rho \vec{u} \Delta H) \qquad (15)$$

Species conservation equation:

The general solute transport equation after transformation can be rewritten as:

$$\frac{\partial}{\partial t}(\rho C) + \frac{\partial}{\partial x}(\rho u C) + \frac{\partial}{\partial y}(\rho v C) + \frac{\partial}{\partial z}(\rho w C)$$
$$= \nabla \cdot (\rho D \nabla C) - \frac{\partial}{\partial x}(\rho u_{scan} C) \qquad (16)$$

where C stands for the mixture concentration.

2.2. Boundary conditions

Since we are performing a single domain analysis for solving the energy and momentum equations, the interface comes out as a solution and there is no need to track the interface and put a boundary condition there. Hence, the boundary conditions for momentum and energy equations are applied on the boundaries of the work-piece domain.

On the top surface, a Gaussian heat flux distribution is assumed, which is given by:

$$q''(r) = \frac{q}{\pi r_q^2} \exp\left(-\frac{r^2}{r_q^2}\right) \qquad (17)$$

where r is the distance from the laser center, and r_q is half the laser beam width. Considering heat losses due

to convection and radiation, the resulting top surface thermal boundary condition becomes

$$-q''(r) + h(T - T_\infty) + \sigma_e \varepsilon (T^4 - T_\infty^4)$$

$$= -k \left(\frac{\partial T}{\partial y} \right)_{top} \qquad (18)$$

The free surface on the top is assumed to remain flat (i.e., $v = 0$). In addition, there would be a balance between shear force and surface tension at the free surface:

$$\tau_{yx} = -\mu \left(\frac{\partial u}{\partial y} \right)_{top} = \frac{\partial \sigma}{\partial T} \left(\frac{\partial T}{\partial x} \right)_{top} \qquad (19)$$

$$\tau_{yz} = -\mu \left(\frac{\partial w}{\partial y} \right)_{top} = \frac{\partial \sigma}{\partial T} \left(\frac{\partial T}{\partial z} \right)_{top} \qquad (20)$$

where σ_T is the temperature coefficient of surface tension.

The bottom face is assumed insulated while the four side faces are subjected to convective heat transfer boundary condition:

$$-k \left(\frac{\partial T}{\partial n} \right)_{wall} = h(T - T_\infty) \qquad (21)$$

where n is in the direction of the outward normal of any side face.

2.2.1. Mass transfer boundary conditions

In each time step, the species conservation Equation 16 is solved after solving the momentum and energy equations. Hence, the current pool boundary along with the velocity and temperature fields are already known. At the top surface, a mass flux of the alloying element (aluminium, in this case) is added in the form of a powder. The particle sizes in the powder are usually in the range of 20–70 microns. Since the temperature of the molten iron base metal is much higher than the melting point of aluminium, it is expected that the powder particles will melt almost instantaneously. Hence, the mass flux of aluminium at the top surface can be assumed to be in a molten state, and represented in the model as a Neumann boundary condition:

$$-D \frac{\partial C}{\partial y} = \dot{m} \qquad (22)$$

where $\dot{m}$ is the mass flux of aluminium distributed uniformly over a circular area of radius r_q. In Equation 22, D is the diffusion coefficient of the alloying element in the molten base material. The mass flux m is assumed to be uniform and is calculated from the powder feed rate (m_f) as:

$$\dot{m} = \left(\frac{m_f}{\pi r_q^2} \right) \qquad (23)$$

The alloying element mixes with the molten base metal by convection and diffusion. At the solidification interface, only a part of solute, $k_p C$, goes into the solid phase, where k_p is the partition coefficient. This happens because the solute is less soluble in the solid phase

than in the liquid phase. As a result, the remaining solute, $(1 - k_p)C$, is rejected back into the liquid. Thus, the solute flux balance at the solidification front is given by:

$$-D \frac{\partial C}{\partial n} = v_n(C)(1 - k_p) \qquad (24)$$

where n is the direction of outward normal, and v_n is the interface velocity in that direction. At the fusion front, the melting solid does not contain the alloying element, which results in an effective dilution of the solute. The resulting boundary condition at the fusion front can be written as:

$$D \frac{\partial C}{\partial n} = -v_n(C) \qquad (25)$$

3. Numerical procedure

The governing equations of mass, momentum and energy conservation are simultaneously solved numerically using a pressure based, fully implicit finite volume technique according to the SIMPLER algorithm [9]. The algorithm is appropriately modified to include the enthalpy-porosity model for the phase change process. The porous-medium source terms in the momentum Equations 6–8 are calculated for any control volume using the value of liquid fraction, f_l, for that particular control volume. The value of liquid fraction is calculated as $f_i = \frac{\Delta H}{L}$, where ΔH, the latent heat content of a particular control volume, is obtained from the solution of the energy conservation equation. In the numerical solution of the energy conservation equation, a special treatment is applied to update the nodal latent heat content. The procedure, which is elaborated in references [8] and [10], is briefly described below. The enthalpy update is governed by the equation:

$$[\Delta H_p]_{n+1} = [\Delta H_p]_n + \frac{a_p}{a_p^0} \lambda \left\{ [h_p]_n - F^{-1}(\Delta H) \right\} \qquad (26)$$

where n Jenotes the iteration level and λ is a relaxation factor. The terms a_p and a_p^0 are the nodal-point coefficient and the coefficient associated with the transient part in the discretised energy equation, respectively.

Numerical computations are performed for the case of laser surface alloying of aluminium on an iron substrate. The corresponding thermophysical properties are listed in Table I. For a mixture, the properties such as thermal conductivity, k, specific heat, c or viscosity, μ are calculated using the following relation:

$$P = P_{Al} C_{Al} + P_{Fe}(1 - C_{Al}) \qquad (27)$$

where P stands for k, c or μ, as the case may be. The process parameters appropriate to the present study are taken as: scanning speed of 0.003 m/s, laser power of 2400 W, efficiency of heat input as 0.15, and a powder feed rate of 0.2 gm/s.

For the numerical simulation, a $48 \times 35 \times 48$ non-uniform grid system is used to discretise a domain having a dimension of 8 mm $\times$ 4 mm $\times$ 8 mm. Typically fine grids are chosen to describe the portion of the domain falling within the molten pool, in order to resolve the melt-pool convection in an effective manner. The time steps for computations are also varied

TABLE I List of physical properties

	Values
Physical properties (constants)	
β_T (for iron)	1.0×10^{-5} K^{-1}
T_m (for iron)	1809.15 K
T_{boil} (for iron)	3133.15 K
L (for iron)	2.47196×10^5 J/kg
ρ (for iron)	7800 kg/m^3
σ (for iron)	-4.9×10^{-4} N/mK
σ (for aluminium)	-3.5×10^{-4} N/mK
Physical properties (variables)	
μ (for iron)	$3.3699 \times 10^{-4} \exp(41400/\bar{R}T)$ Nm/s^2
μ (for aluminium)	$1.492 \times 10^{-4} \exp(16500/\bar{R}T)$ Nm/s^2
k (for iron)	
273 $K \leq T \leq 373$ K	78.2 W/mK
373 $K \leq T \leq 1890$ K	41.0 W/mK
$T \geq 1809$ K	44.0 W/mK
k (for aluminium)	
273 $K \leq T \leq 373$ K	238.0 W/mK
373 $K \leq T \leq 993$ K	231.4 W/mK
$T \geq 993$ K	109.3 W/mK
c (for iron)	
273 $K \leq T \leq 373$ K	456.0 J/kgK
373 $K \leq T \leq 1890$ K	658.6 J/kgK
$T \geq 1809$ K	804.0 J/kgK
c (for aluminium)	
273 $K \leq T \leq 373$ K	971 J/kgK
373 $K \leq T \leq 993$ K	1049.2 J/kgK
$T \geq 993$ K	1212.0 J/kgK

according to the stages of the melting process. During the conduction phase, large time steps (about 0.005 s) are allowed until melting begins (typically after 0.01 s). Once melting starts, the high temperature gradients in the pool set up a strong Marangoni convection, leading to high fluid velocities of the order of 1 m/s within

a very short time. Hence, time steps during the initial stages of pool development are chosen to be very small (about 0.0005 s). After the molten pool reaches a more developed stage, larger time can be chosen in order to save computation time. Finally, computation is carried until a quasi-steady state is reached. It is found that a further refinement in the grid-size or time-step does not alter the results appreciably.

4. Results and discussion
4.1. Nature of velocity and temperature fields

Figs 2–4 show the velocity fields in the three different views. A loop of very high velocity is found to exist immediately adjacent to the top surface of the pool. This flow is induced by the surface tension gradient (Marangoni convection) at the surface of the pool. For the present case, the surface tension is a decreasing function of temperature. As a result, liquid metal near the centre of the pool is pulled towards the relatively cooler pool edges, resulting in counter-rotating vortices as shown in Fig. 4. After the hot liquid metal from the pool centre reaches the edge, it turns downwards and provides a "digging" effect at the solid-liquid interface, as observed in Figs 6 and 7. Convection effects thus significantly alters the shape and size of the pool. The present transient phase change model allows us to capture the evolution of the pool development until it reaches a quasi-steady state. Hence, it considers the direct effect of convection in the evolutionary development of the pool geometry, which is a more realistic representation of the physical phenomenon. It is clear from Fig. 4 that, because of very high convection
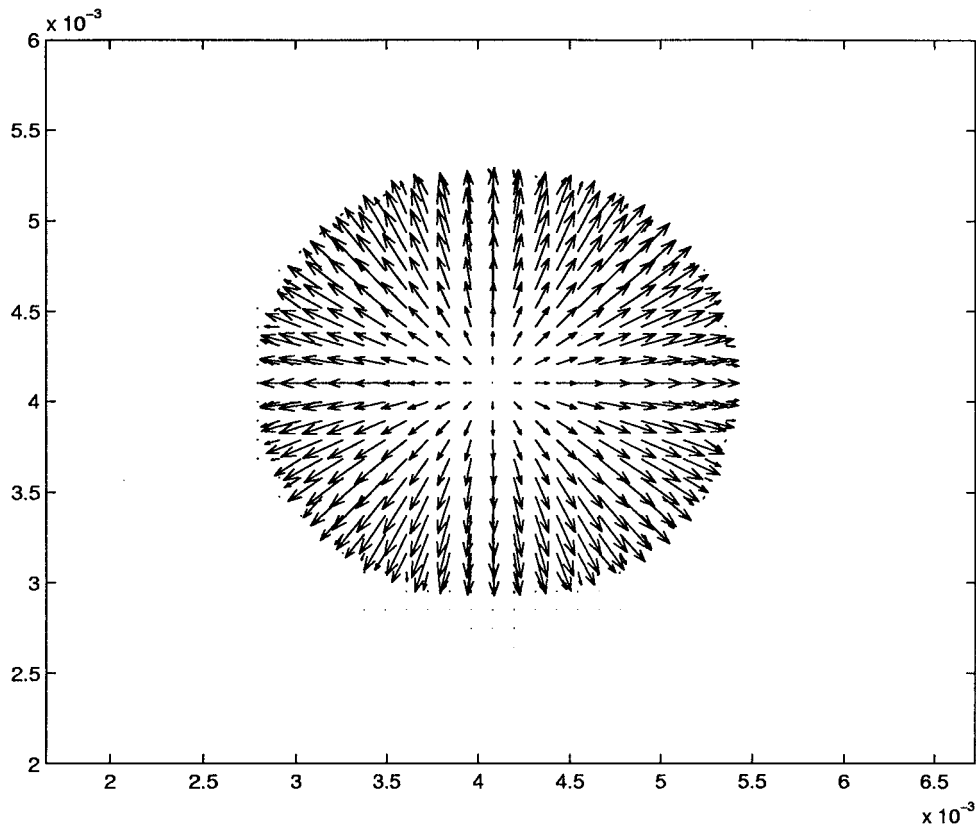
Figure 2 Velocity vector plot (top view) for the case of $u_{scan} = 0.003$ m/s, power $= 2400$ W, $\eta = 0.15$ and powder feedrate $= 0.02$ gm/s. All dimensions are in m.
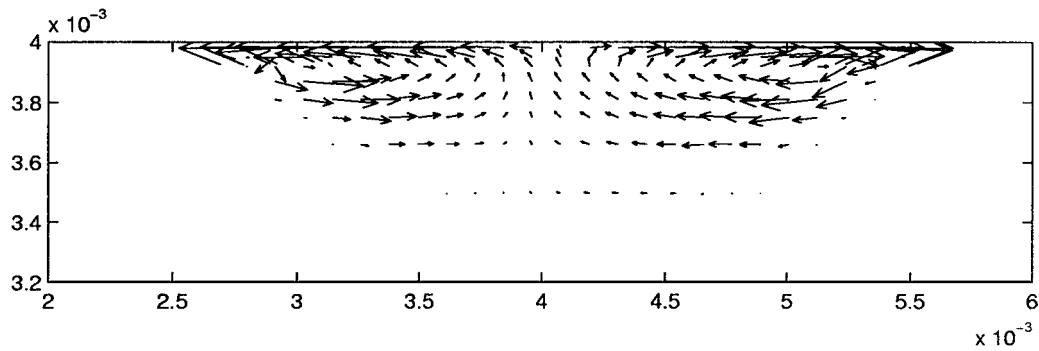
Figure 3 Velocity vector plot (longitudinal sectional view) for the case of $u_{scan} = 0.003$ m/s, power $= 2400$ W, $\eta = 0.15$ and powder feedrate $= 0.02$ gm/s. All dimensions are in m.
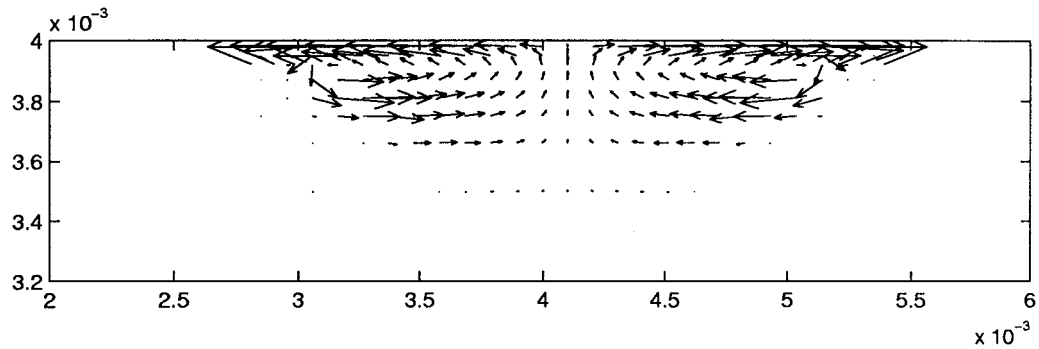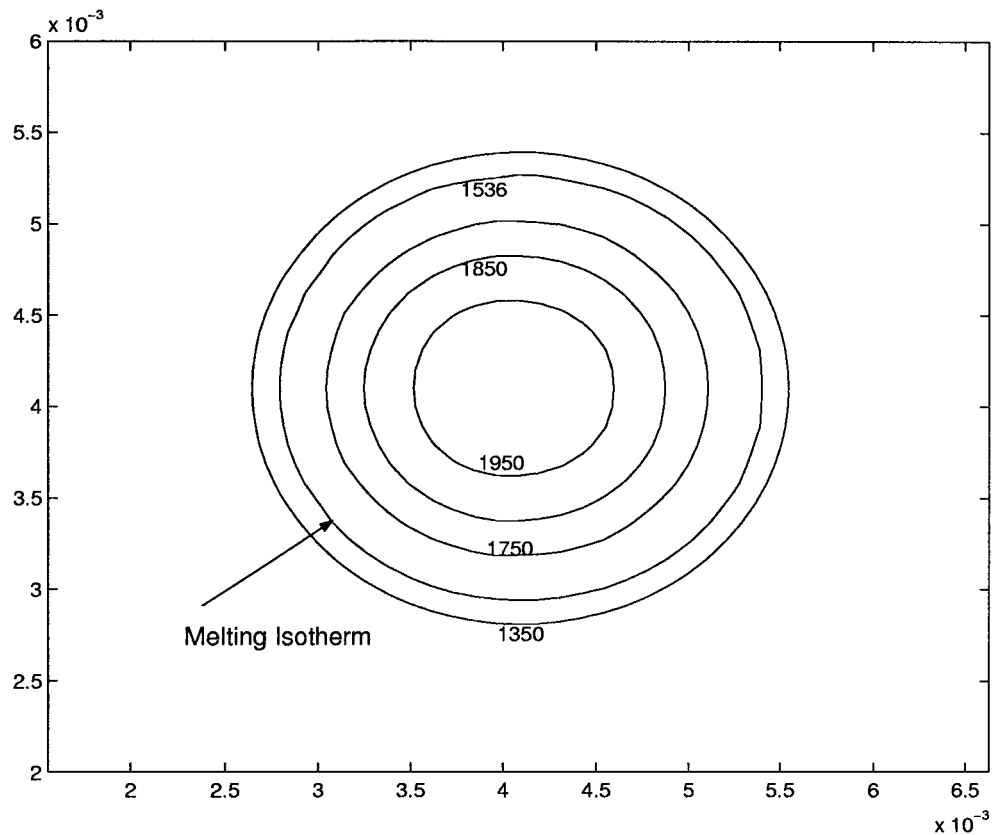

Figure 4 Velocity vector plot (cross sectional view) for the case of $u_{scan} = 0.003$ m/s, power $= 2400$ W, $\eta = 0.15$ and powder feedrate $= 0.02$ gm/s. All dimensions are in m.

Figure 5 Temperature contours (top view) for the case of $u_{scan} = 0.003$ m/s, power $= 2400$ W, $\eta = 0.15$ and powder feedrate $= 0.02$ gm/s. All dimensions are in m.

(radially outward) at the top surface, the shape of the pool becomes wider and shallower.

4.2. Distribution of solute concentration

The iso-concentration plots of the species in the molten pool in three planes are shown in Figs 8–10. It is ob-

served from Figs 8 and 9 that the concentration is maximum at the solidification front and gradually decreases towards the melting front. At the melting front, there is always a dilution of species due to addition of fresh molten base metal. On the other hand, due to the less solubility of the solute in the solid phase than in the
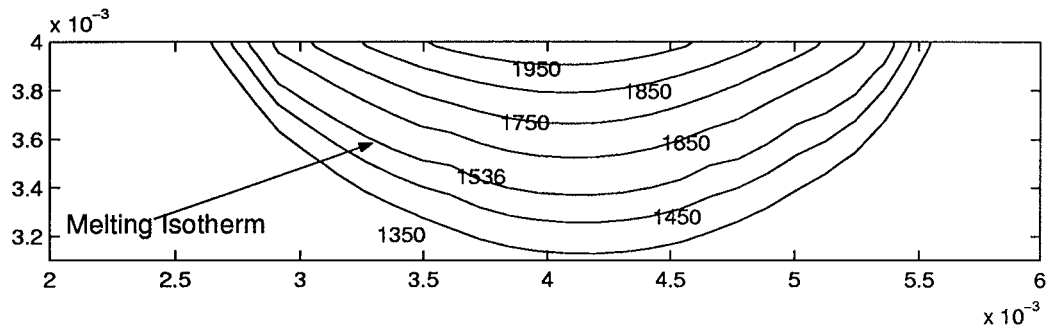
Figure 6 Temperature contours (longitudinal sectional view) for the case of $u_{scan} = 0.003$ m/s, power $= 2400$ W, $\eta = 0.15$ and powder feedrate $= 0.02$ gm/s. All dimensions are in m.
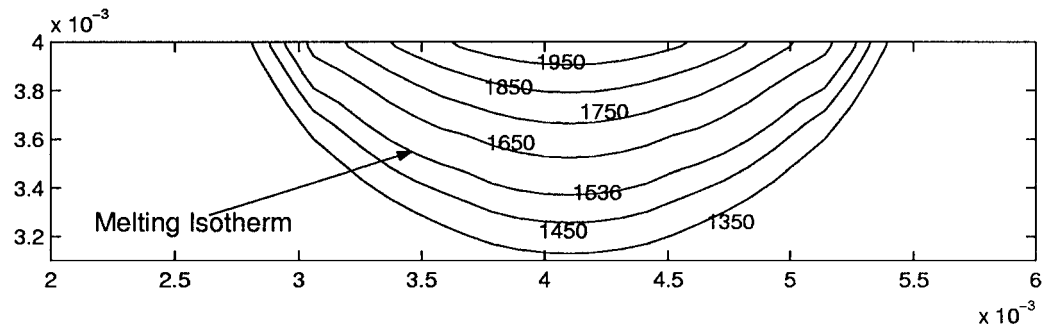

Figure 7 Temperature contours (cross sectional view) for the case of $u_{scan} = 0.003$ m/s, power $= 2400$ W, $\eta = 0.15$ and powder feedrate $= 0.02$ gm/s. All dimensions are in m.

liquid phase, there will be solute rejection from the solidified material back into the molten pool at the solidification front. As evident from the velocity vectors in the longitudinal plane (Fig. 3), there is a continuous flow of material from the solidification front towards the melting front Hence, iso-concentration lines are more closely packed at the melting front leading to higher concentration gradient.

4.3. Variation of cooling rate

To calculate cooling rate, we use the transformation equation which is given by:

$$
\frac{\partial}{\partial t}(\phi(x', y, z, t)) = \frac{\partial}{\partial t}(\phi(x, y, z, t))
$$
$$
+ u_{scan}\frac{\partial}{\partial x}(\phi(x, y, z, t)) \tag{28}
$$

where the general variable ϕ stands for temperature, T, in the present case. From the quasisteady temperature field, one can obtain the variation of temperature with space and time. By making use of the transformation Equation 28, this variation can be expressed as:

$$
T(x', y, z, t_2) = T(x', y, z, t_1)
$$
$$
+ \frac{T(x_2, y, z) - T(x_1, y, z)}{x_2 - x_1} u_{scan}(t_2 - t_1) \tag{29}
$$

where $T(x_2, y, z)$ and $T(x, y, z)$ are the steady-state temperatures at two different x-locations and $(t_2 - t_1)$ is the time required by the laser beam to travel a distance of $(x_2 - x_1)$ with a constant speed, u_{scan}. Using Equation 29, we can calculate the cooling rate at any location of the working domain. From microstructural point of view, the cooling rate at the solidification front,

which is plotted in Fig. 11, plays a significant role. As evident from Fig. 11, the order of magnitude of the cooling rate is typically very high (10^4 K/s). Fine microstructures usually observed in laser processing are attributed to such high cooling rates [11, 12]. We also observe that the cooling rate is maximum near the top surface where hot fluid from the pool centre is transported to the solidification interface by convection.

4.4. Comparison with experiments

For the purpose of qualitative validation of our model, we have made some comparisons with the corresponding experimental studies. Aluminium powder is added to the molten pool of an iron substrate, the composition of which is given in Table II. Fig. 12 shows the microstructure of a cross section of the alloyed region. The pool shape depicted in Fig. 12 shows a good qualitative agreement with the numerically predicted shape shown in Fig. 6.

The solute concentration distribution in the solidified alloy can be determined from the concentration distribution at the solidification front. Since the solubility of the solute in the solid phase is less than that in the

TABLE II Composition of substrate used in the experiments

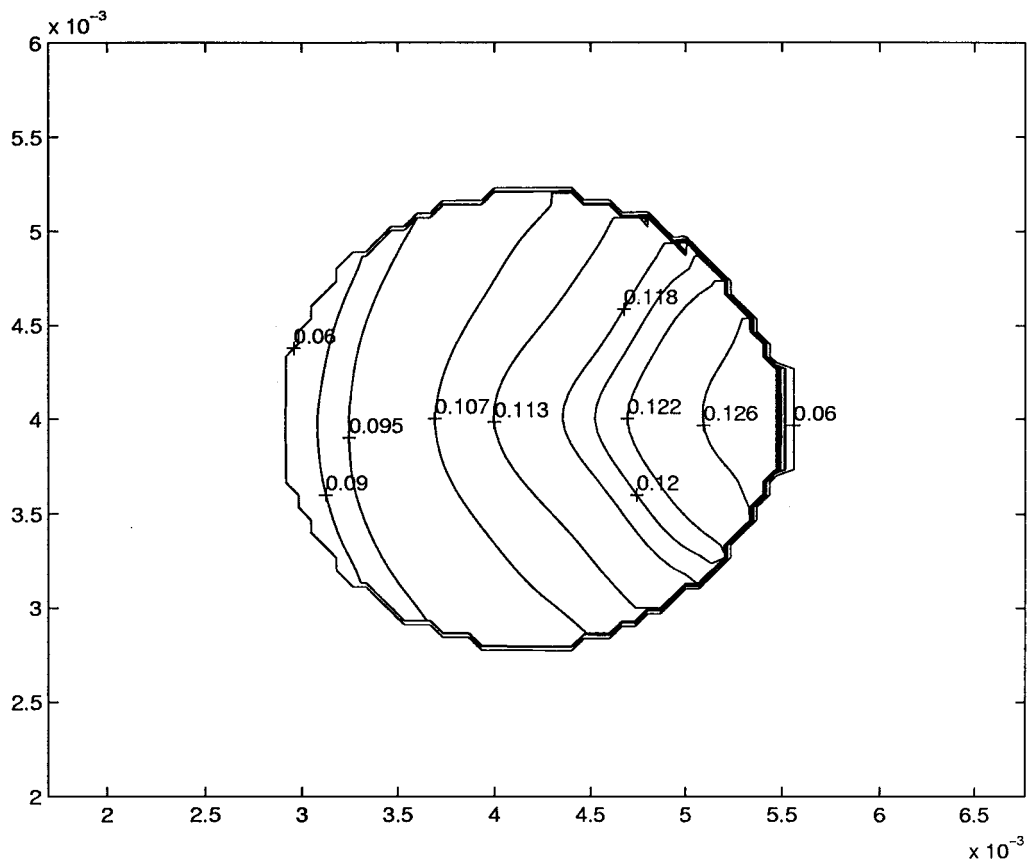| Element	wt%
C	0.024
Si	0.004
Mn	0.048
S	0.012
P	0.006
Cr	0.001
Ni	0.003
Mo	0.001
Fe	Balance

161

Figure 8 Solute concentration contours in the molten pool in terms of mass fraction of aluminium (top view) for the case of $u_{scan} = 0.003$ m/s, power $= 2400$ W, $\eta = 0.15$ and powder feedrate $= 0.02$ gm/s. All dimensions are in m.
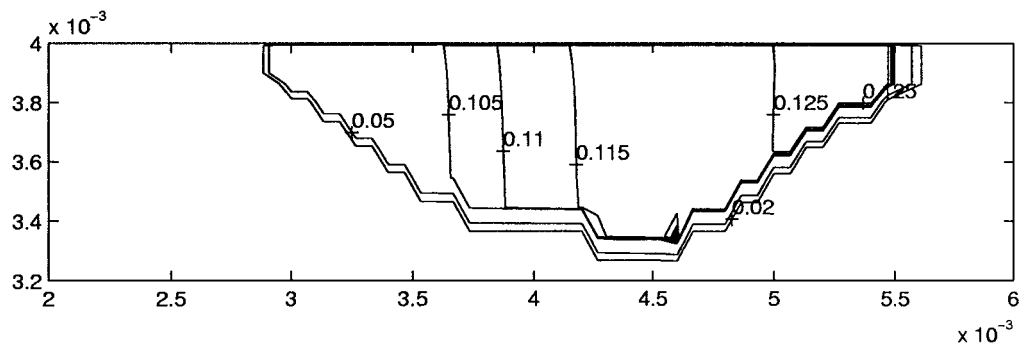

Figure 9 Solute concentration contours in the molten pool in terms of mass fraction of aluminium (longitudinal sectional view) for the case of $u_{scan} = 0.003$ m/s, power $= 2400$ W, $\eta = 0.15$ and powder feedrate $= 0.02$ gm/s. All dimensions are in m.
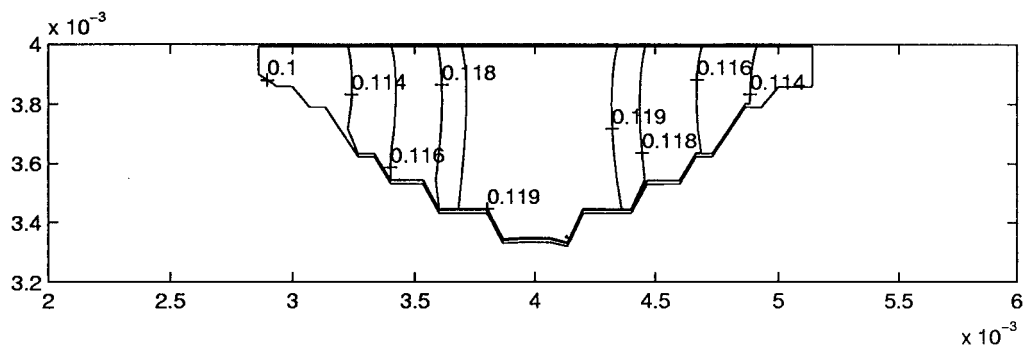

Figure 10 Solute concentration contours in the molten pool in terms of mass fraction of aluminium (cross sectional view) for the case of $u_{scan} = 0.003$ m/s, power $= 2400$ W, $\eta = 0.15$ and powder feedrate $= 0.02$ gm/s. All dimensions are in m.

liquid phase, the solute enters the solid phase with a concentration of k_pC. If we multiply the species concentration at any point on the solidification front (in the longitudinal section shown in Fig. 9) by k_p and then map it on a vertical line, we can numerically predict the concentration variation with depth along the centreline of the solidified material. This prediction is shown in Fig. 13. It is observed from Fig. 13 that concentration increases with height from the bottom. Near the top surface. concentration is almost uniform, due to mixing
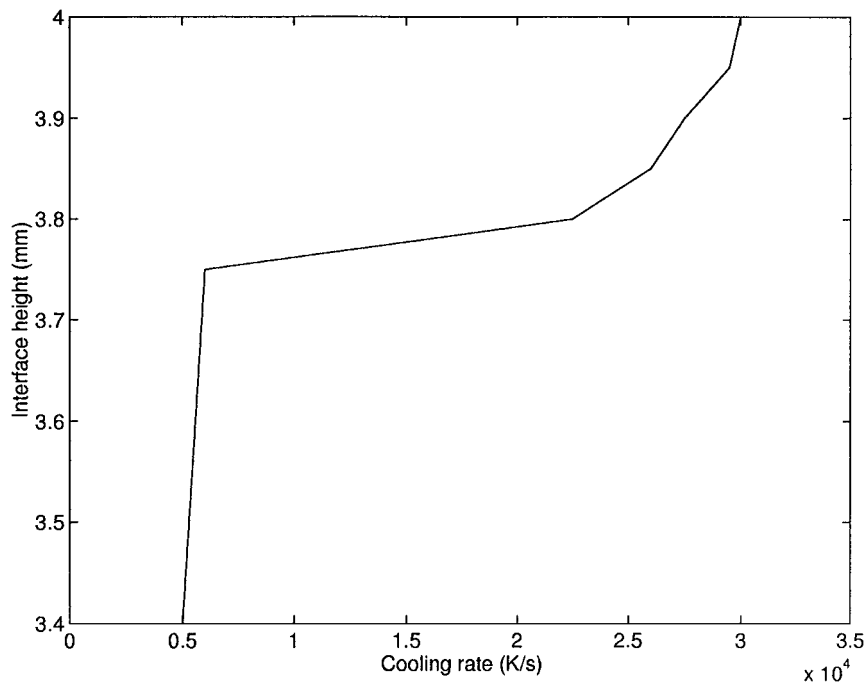
Figure 11 Variation of cooling rate of the solidification interface in the longitudinal plave along the laser centreline.
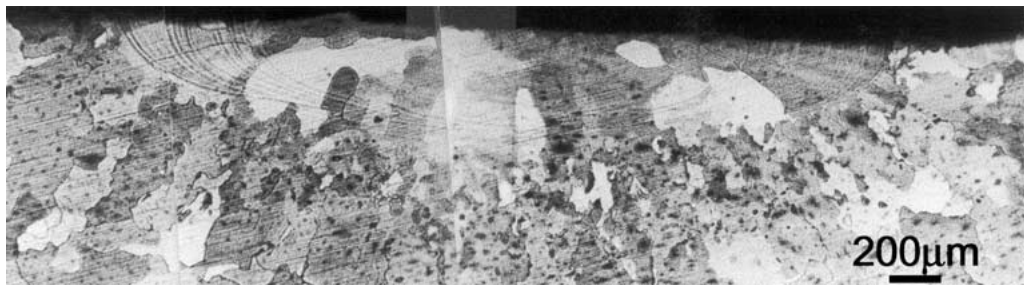

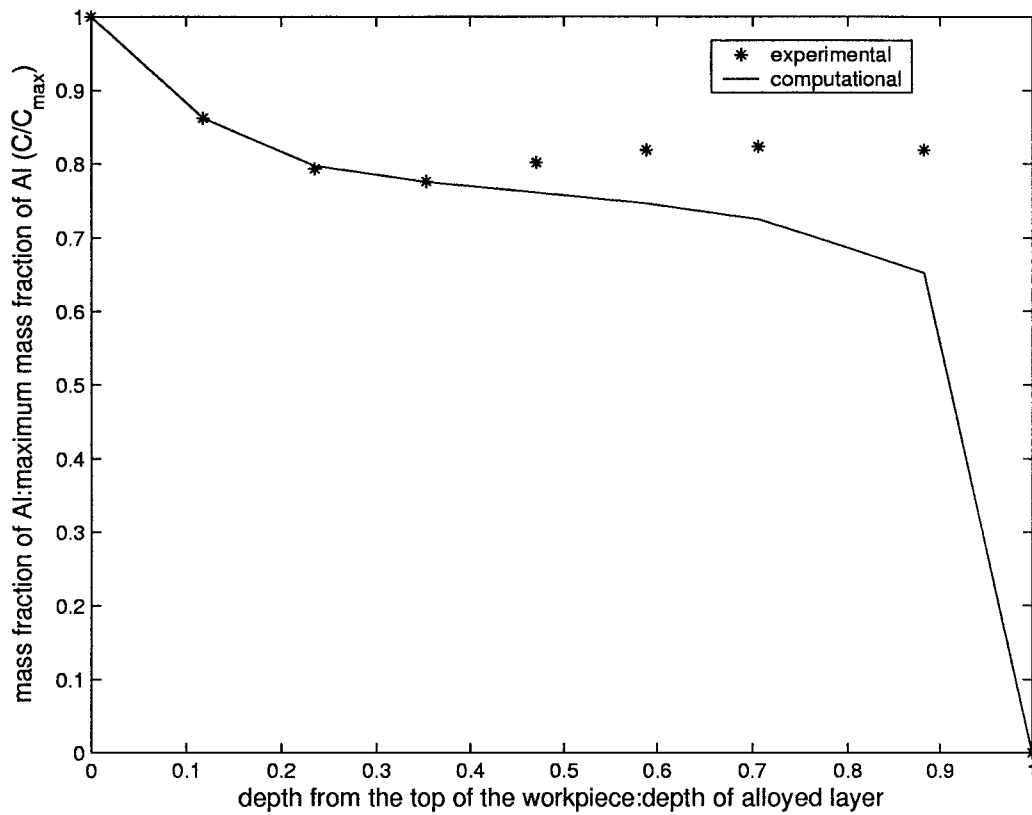*Figure 12* Microstructure of the alloyed layer.

Figure 13 Comparison of experimental results and numerical predictions regarding solute concentration variation (in terms of mass fraction of aluminium) with depth from the top surface along the solidification interface.

caused by strong convection loops. The corresponding experimental results are also shown in Fig. 13, revealing a good qualitative agreement with the numerical results.

5. Conclusions

A three dimensional transient model is developed for predicting the transport phenomena in laser surface alloying. It is found that the final pool geometry predicted by this transient model is different from the ones generated by previous quasi-steady models reported in the literature. The results also show that the pool geometry and flow dynamics are inherently three dimensional in nature, and hence cannot be accurately represented by two-dimensional or axi-symmetric models existing in the literature. The three-dimensional model is also able to predict the species composition distribution in the entire cross section of the solidified alloy, a feature which is extremely important from metallurgical and process design point of view. The model also calculates the variation of cooling rate along the solidification interface. The numerical predictions are finally compared with the corresponding experimental results with regard to pool shape and final composition distribution, and a good agreement can be observed.

References

1. C. L. CHAN, J. MAZUMDAR and M. M. CHEN, *Materials Science and Technology* **3** (1987) 306.
2. *Idem., Metall. Trans.* A **15** (1984) 2175.
3. *Idem., J. Appl. Phy.* **64** (1988) 6166.
4. B. BASU and J. SRINIVASAN, *Int. J. Heat Mass Transfer* **31** (1988) 2331.
5. S. KOU and Y. H. WANG. *Metall. Trans.* A **17** (1986) 2265.
6. J. C. CHEN and Y. C. HUANG, *Int. J. Heat Mass Transfer* **34** (1990) 663.
7. X. HE, B. L. MORDIKE, N. PIRCH and E. W. KREUTZ, *Lasers in Engineering* **4** (1995) 291.
8. A. D. BRENT, V. R. VOLLER and K. J. REID, *Num. Heat Transfer* A **13** (1988) 297.
9. S. V. PATANKAR, in "Numerical Heat Transfer and Fluid Flow" (Hemisphere, Washington D.C., 1980).
10. V. R. VOLLER and C. PRAKASH, *Int. J. Heat Mass Transfer* **30** (1987) 1709.
11. G. PHANIKUMAR, B. BASU, S. CHAKRABORTY, K. CHATTOPADHYAY, P. DUTTA and J. MAJUMDER, in Proceedings of EUROMAT'99, Vol. 11 (Wiley-VCH, Berlin, 2000).
12. K. K. PRASANT, K. CHATTOPADHYAY and J. MAJUMDER, *J. Mater. Sci.* **34** (1999) 3437.